Materials Research. 2019; 22(3): e20190078
DOI: http://dx.doi.org/10.1590/1980-5373-MR-2019-0078

Crystallization Behavior and Mechanical Properties of Cu-based Bulk Metallic Glass Composites

***Ge Wang*[a], *Boyu Jiang*[a], *Xingguo Zhang*[a]*, *Bingwen Zhou*[a], *Linggang Meng*[a]**

[a]*School of Materials Science and Engineering, Dalian University of Technology, Dalian 116024, China*

Received: January 29, 2019; Revised: April 04, 2019; Accepted: April 09, 2019

This work highlights the relationship between the preparation, crystallization behavior, microstructures, and mechanical properties of Cu-based bulk metallic glasses (BMGs) and their composites (BMGCs). $(Cu_{47}Zr_{45}Al_8)_{97.5}Y_{1.5}Nb$ in-situ BMGCs were prepared using isothermal annealing, and the experimental results indicate tunable mechanical properties of the alloys by processing parameter manipulation. The crystallinity of $(Cu_{47}Zr_{45}Al_8)_{97.5}Y_{1.5}Nb$ BMGCs increases with extended annealing temperature and time, while their phase transition with rising temperature follows Am (amorphous state) → Am + $Cu_{10}Zr_7$ →Am + $Cu_{10}Zr_7$ + $AlCu_2Zr$ + Al_2Zr. Precipitation strengthening during annealing above 720 K (447 ºC) can enhance the alloy microhardness remarkably and achieve an optimum of 712 HV by annealing at 800 K (527 ºC) for 60 min. TEM results show that $Cu_{10}Zr_7$ with sizes of 12~15 nm precipitates out upon crystallization and thereby accounts for the superior compressive property. The alloy exhibits a fracture strength up to 2080 MPa after annealing at 680 K (407 ºC) for 30 min. Morphological observation of the fracture surface reveals a transition of fracture characteristics from the typical amorphous ductile manner to a brittle manner with further annealing. The investigation provides novel thoughts of BMGs processing for further performance improvement.

Keywords: *Cu-based BMGCs, isothermal annealing, crystallization behavior, mechanical properties.*

1. Introduction

As an emerging class of advanced materials with huge potentials in technological benefits, bulk metallic glasses (BMGs) possess unique fracture mechanisms and superior mechanical properties such as ultra-high strength, high fracture toughness, low elastic modulus, and high hardness[1-5]. Numerous efforts have been given nowadays to develop diversiform BMG systems with enhanced functionality and improved mechanical performance, so as to better meet the requirements of structural and engineering materials[6-8]. However, most BMG systems are tightly restrained from broad applications due to their insufficient glass forming ability (GFA) and costly fabrication[9]. Among them, the Cu-Zr system stands out for its ultrahigh strength, high hardness, great GFA (i.e. generally, compressive $\sigma_f \geq 1.5$GPa; $H_v \geq 500$; critical diameter ≥15 mm), and low preparation expense, thereby possessing much application value in the field of engineering[4,9].

Development of new strengthening and toughening methods for BMGs by uncomplicated process is an urgent problem in amorphous alloy field, for which the advent of in-situ nanophase reinforced BMGCs provides a novel way. For instance, BMGCs can be prepared with in-situ crystals by controlling the partial crystallization of BMGs[10-13], of which the enhancement mechanism might be well expounded via scrutinizing the crystallization behavior. Faith et al. inspected the Cu-Zr-Al-Sm system during annealing and confirmed that when annealing at 703 K (430 ºC), Cu_2Sm nanocrystals (5 nm) precipitated out upon crystallization but got restricted for further growth (up to 10 nm) despite the continuous annealing[14]. Correlating the microstructure of $Zr_{48}Cu_{36}Ag_8Al_8$ BMGCs with annealing temperature, Sun et al. investigated the separation of amorphous phase after isothermally annealing at 703 K for 20 min that conduced to generating the $AlZr_2$ and $AlAg_3$ precipitated nanophases at higher annealing temperatures[15]. Moreover, delicate control of partial crystallization may a play positive role on overcoming the room-temperature brittleness of BMGs. Based on the stress-induced transformation method, Liu et al. prepared $Ti_{57.3}Zr_{19.6}Cu_{4.7}Ni_{2.8}Be_{12}Nb_{3.6}$ BMGCs in-situ that showed high tensile plasticity up to 5.5% and significant work-hardening capacity; further, they investigated detailedly the martensitic-transformation-dominated toughening as well as the mechanical twinning phenomenon[16].

Even with great engineering application potential, scarce work has been done to date on comprehensively analyzing the microstructure evolution, mechanical properties, and room-temperature compressive fracture mechanism of Cu-based BMGCs under different isothermal annealing conditions. Thus, in the present work, we have focused particularly on the crystallization processes of $(Cu_{47}Zr_{45}Al_8)_{97.5}Y_{1.5}Nb$ amorphous composites and examined the effects of various annealing parameters on alloys' mechanical properties as well as fracture mode evolution.

*e-mail: zxgwj@dlut.edu.cn

2. Experimental Procedures

Alloy ingots of $(Cu_{47}Zr_{45}Al_8)_{97.5}Y_{1.5}Nb$ in at. % were prepared by arc melting of Cu (99.9 wt. %), Zr (99.9 wt. %), Al (99.99 wt. %), Y (99.9 wt. %), Nb (99.5 wt. %) under Ti-gettered argon atmosphere. Master alloy ingots with uniform composition were melted for 4 times to ensure chemical homogeneity. Next, $(Cu_{47}Zr_{45}Al_8)_{97.5}Y_{1.5}Nb$ amorphous rods with 3 mm in diameter were prepared by copper-mold injection casting; To ensure a lower porosity, the length of these rods was limited to 60~70 mm. Specimens for compression test were cut into an aspect ratio of 2:1, while those for metallographic observation were 0.8 mm in thickness. Then the un-treated specimens were sealed into a quartz tube, evacuated to 6×10^{-3}Pa, isothermally annealed for 600 s at different temperatures, and then quenched into water. Thermal stability of the samples was examined using differential scanning calorimetry (DSC) at a heating rate of 40 K/min. The liquidus (T_l) of the alloys was measured by a differential thermal analyzer (DTA) at a heating rate of 20 K/min. The amorphous and crystalline nature were identified via X-ray diffraction (XRD) with Cu Kα. The observations on nanoscale were carried out via backscattered electron (BSE) and transmission electron microscopy (TEM), all specimens for TEM were prepared via Focus Ion Beam (FIB) microscope. The element proportions of crystals were confirmed by an Energy Dispersive Spectrometer (EDS). The specimens were etched, and then observed by optical microscopy (OM) to investigate the distribution of precipitates. Microhardness of alloys was examined by a Vickers hardness tester with a load of 5 N and time of 10 s. Uniaxial compression tests were performed on a universal testing machine with the strain rate equal to 5×10^{-4} s^{-1}, and the fracture surface was subsequently observed by a scanning electron microscopy (SEM).

3. Results

3.1 Crystallization analysis

The thermodynamic parameters for $(Cu_{47}Zr_{45}Al_8)_{97.5}Y_{1.5}Nb$ and several relevant BMGs were determined via DSC and DTA analysis as shown in Figure 1. The thermodynamic parameters and critical diameter (Dc) of the alloy and several other relevant compositions are listed in Table 1. Thus, referring to the T_x value obtained, annealing temperatures of 680 K, 700 K, 720 K, 740 K, and 760 K (407 ºC, 427 ºC, 447 ºC, 467 ºC, and 487 ºC) near the supercooled liquid zone were selected for the fine control of partial crystallization within $(Cu_{47}Zr_{45}Al_8)_{97.5}Y_{1.5}Nb$ samples.

Phase structures of the alloy samples are vastly influenced by annealing temperature. With the treatment time fixed at 30 min, XRD patterns corresponding to lower-temperature [i.e. temperature lower than 720 K (447 ºC)] annealing only exhibit amorphous diffuse humps that are typically associated with the amorphous structures (Figure 2 (a)). With the annealing temperature raised to 740 K (467 ºC), slight crystalline peaks show up on the top of the amorphous hump, and sharp crystalline peaks appear when further heating up to 760 K (487 ºC), indicating that the crystallization phase has been extensively formed within the alloy. As the thermal treatment extended to 60 min, the temperature at which crystalline diffraction peaks appear decreases from 760 K (487 ºC) to 740 K (467 ºC) (Figure 2 (b)). Moreover, the specific process of phase transition is analyzed with the XRD patterns related to 60 min annealing, which suggest $Cu_{10}Zr_7$ (Aba2) as the primary phase after 740 K annealing while $Cu_{10}Zr_7$ (C2ca), $AlCu_2Zr$ (Fm3m), and Al_2Zr (P63/mmc) as the main precipitate components after 760 K treatment.

Distributions of the nano-size precipitated phases were further investigated by BSE and OM, given the incapability of XRD technique. Figure 3 presents the BSE micrographs for the precipitated phases with amorphous matrix after annealing at 680 K (407 ºC) and 700 K (427 ºC). There are nano-crystals with the size of 20~100 nm existing in the matrix (Figure 3 (a) and (b)), and the phase composition is identified as $Cu_{10}Zr_7$ using EDS analysis. Besides, a few Y_2O_3 crystals with the size of 200~300 nm are also observed gathering at a few areas due to the inevitable oxygen doping during experiments (Figure 3 (c)). OM graphs reveal clearly the homogeneous distribution of precipitated $Cu_{10}Zr_7$ phases after thermal treatment, and Figure 4 (a)~(e) depict the rapid increment in phase number density as raising the annealing temperature from 680 K (407 ºC) to 760 K (487 ºC). However, we also notice that deficiency in the atomic activity can largely inhibit phase growth. Figure 4 (f) demonstrates the follow-up growth of $Cu_{10}Zr_7$ phases when annealing at 780 K (507 ºC), in which drastic crystallization related to the crystalline peaks in Figure 2 (a) and agglomeration regions of $Cu_{10}Zr_7$ are well presented in the matrix.

TEM observations are carried out for a more detailed analysis of the sizes and compositions of the precipitates. The featureless bright field (BF) image, the halo ring shown in SAED (Figure 5 (a)) and HRTEM (Figure 5 (b)) indicate the amorphous nature of the matrix. The BF image (Figure 5 (c)) and HRTEM (Figure 5 (d)) confirm the presence of crystals with 12~15 nm mean sizes precipitated on the matrix after annealing at 680 K for 30 min. After annealed at 700 K for 30 min, the growth of these crystals are observed, the BF image (Figure 5 (e)) and HRTEM (Figure 5 (f)) show

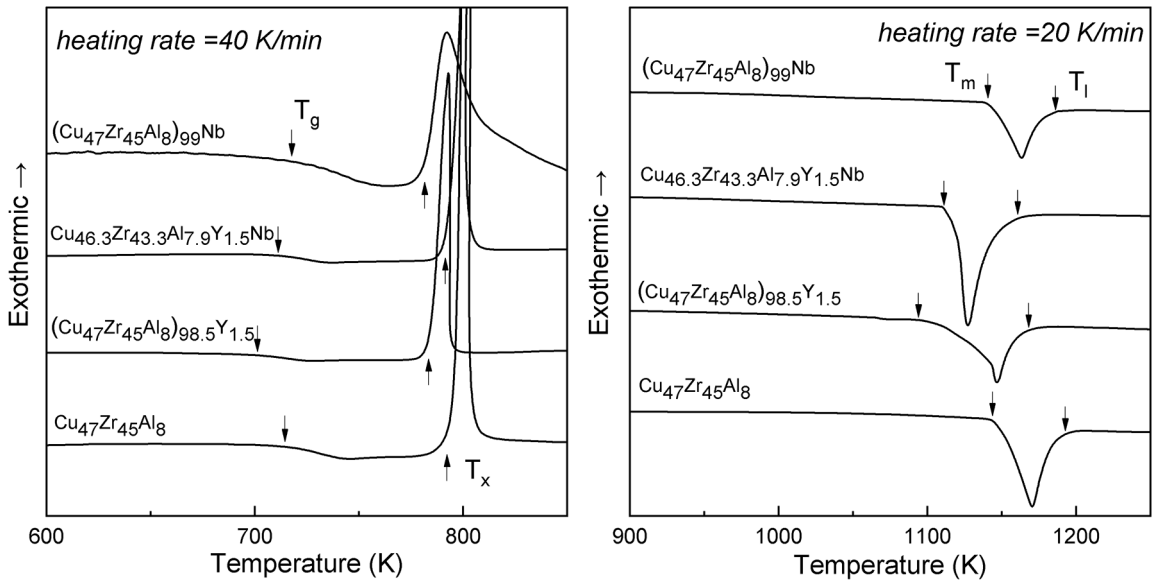

Figure 1. DSC and DTA curves of several relevant compositions of Cu-Zr-Al systems.

Table 1. Thermodynamic parameters and D_c of several compositions of Cu-Zr-Al system

	T_g(K)	T_x(K)	ΔT_x(K)	T_l(K)	T_{rg}	γ	D_c(mm)
$Cu_{47}Zr_{45}Al_8$	714	794	80	1190	0.600	0.417	15
$(Cu_{47}Zr_{45}Al_8)_{98.5}Y_{1.5}$	698	783	85	1168	0.598	0.420	25
$(Cu_{47}Zr_{45}Al_8)_{99}Nb$	717	790	73	1185	0.605	0.415	12
$(Cu_{47}Zr_{45}Al_8)_{97.5}Y_{1.5}Nb$	710	793	83	1161	0.611	0.423	18

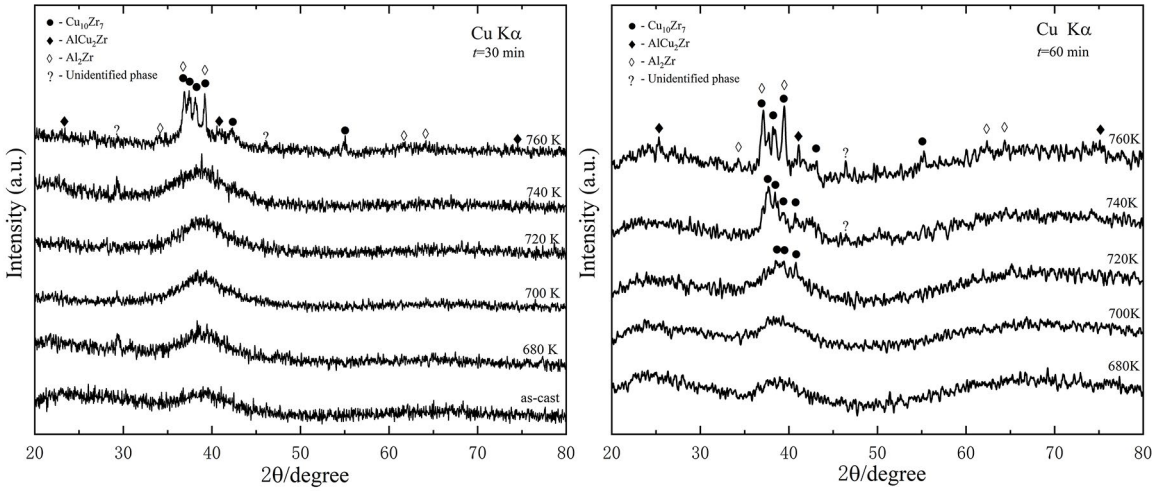

Figure 2. XRD patterns of annealed $(Cu_{47}Zr_{45}Al_8)_{97.5}Y_{1.5}Nb$ alloys: (a) 30 min; (b) 60min.

evidently the crystals precipitate with 21~26 nm mean sizes and are identified as $Cu_{10}Zr_7$ via the FFT (inset of Figure 5 (f)).

3.2 Microhardness testing

Generally, microhardness testing enables convincing analysis about the deformation resistance of alloys. Figure 6 summarizes the variation of Vickers hardness after $(Cu_{47}Zr_{45}Al_8)_{97.5}Y_{1.5}Nb$ BMGCs have undergone different annealing procedures. For the lower annealing temperature of 680 K (407 ºC), the sample hardness reaches 546 HV and 570 HV after 30 min and 60 min, respectively. Elevated temperature leads to much enhanced Vickers hardness,

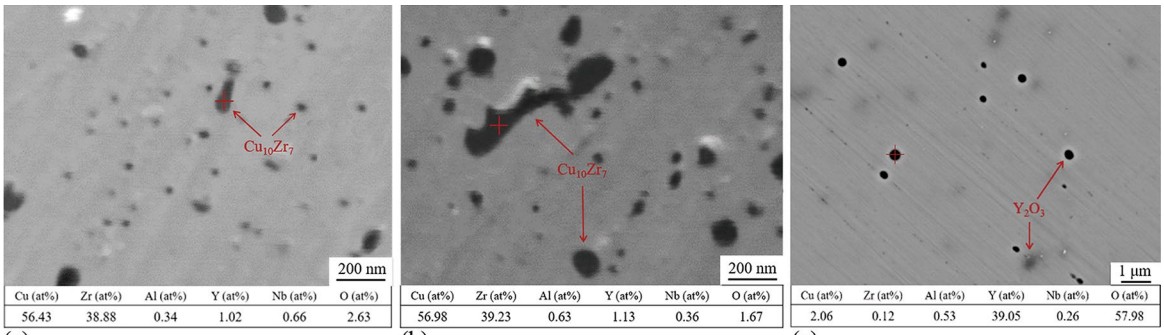

Figure 3. BSE micrographs and corresponding EDS results of nanocrystalline phases of $(Cu_{47}Zr_{45}Al_8)_{97.5}Y_{1.5}Nb$ alloys after annealing: (a) 680 K; (b) 700 K; (c) Distribution of Y_2O_3 (700 K).

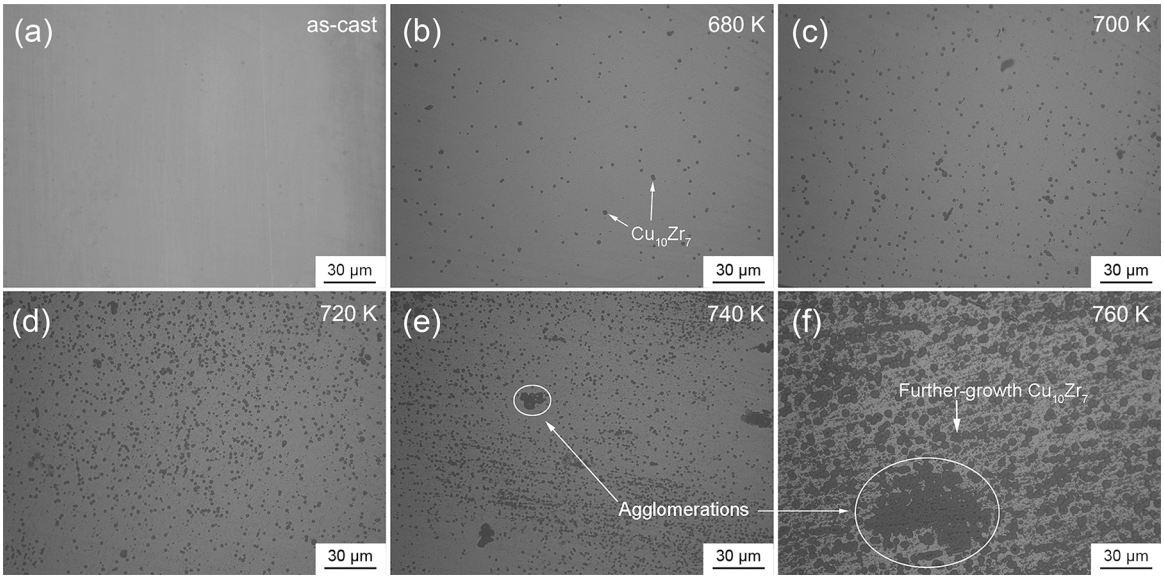

Figure 4. OM micrographs of $(Cu_{47}Zr_{45}Al_8)_{97.5}Y_{1.5}Nb$ alloys annealed at different temperatures for 30 min: (a) as-cast; (b) 680 K; (c) 700 K; (d) 720 K; (e) 740 K; (f) 760 K.

which reaches 706 HV and 712 HV at 800 K (527 ºC), an increase of 31% and 32% in comparison with the results of as-cast samples. Apparently, the two data series that represent two annealing periods enter the fast growth zone at 740 K (467 ºC) and 760 K (487 ºC), respectively, which correspond to the extensive appearance of crystalline peaks in Figure 2. Therefore, the microhardness enhancement should be ascribed to the highly crystallized matrix as shown by the OM micrographs in Figure 5.

3.3 Compressive property and fracture mode evolution

$(Cu_{47}Zr_{45}Al_8)_{97.5}Y_{1.5}Nb$ alloys annealed for 30 min but at different temperatures were subjected to uniaxial compression tests, and the compressive stress-strain curves are plotted in Figure 7 accordingly. While the fracture strength of fully amorphous sample equals 1970 MPa, that of the alloy annealed at 680 K (407 ºC) rises to 2080 MPa. However, upon elevating the annealing temperature to 700 K (427 ºC) and 720 K (447 ºC), fracture strength of the samples reduces to 1840 MPa and 1810 MPa, respectively, and a little plastic strain of 0.3% can be observed for the latter. Further temperature increase leads to a remarkable downtrend in fracture strength, with 1320 MPa and 730 MPa obtained in the 740 K (467 ºC) case and 760 K (487 ºC) case, respectively. The annealing temperature of 760 K (487 ºC) made alloy fracture into sheets and filaments directly in the process of elastic deformation.

According to the SEM micrographs of compressed fractures, the shear fracture characteristics (~45°) can be well maintained for the samples annealed at 680 K (407 ºC) and 700 K (427 ºC) (Figure 8(a) and (b)); these two samples share similar fracture morphology, in which the typical vein patterns are extensively and homogeneously distributed. Such observation can be ascribed to the release of electric energy, which has been heavily accumulated before fracture, that generates a local melting zone in the shear bands[17]. Nevertheless, Figure 8 (a) reveals a distinctly

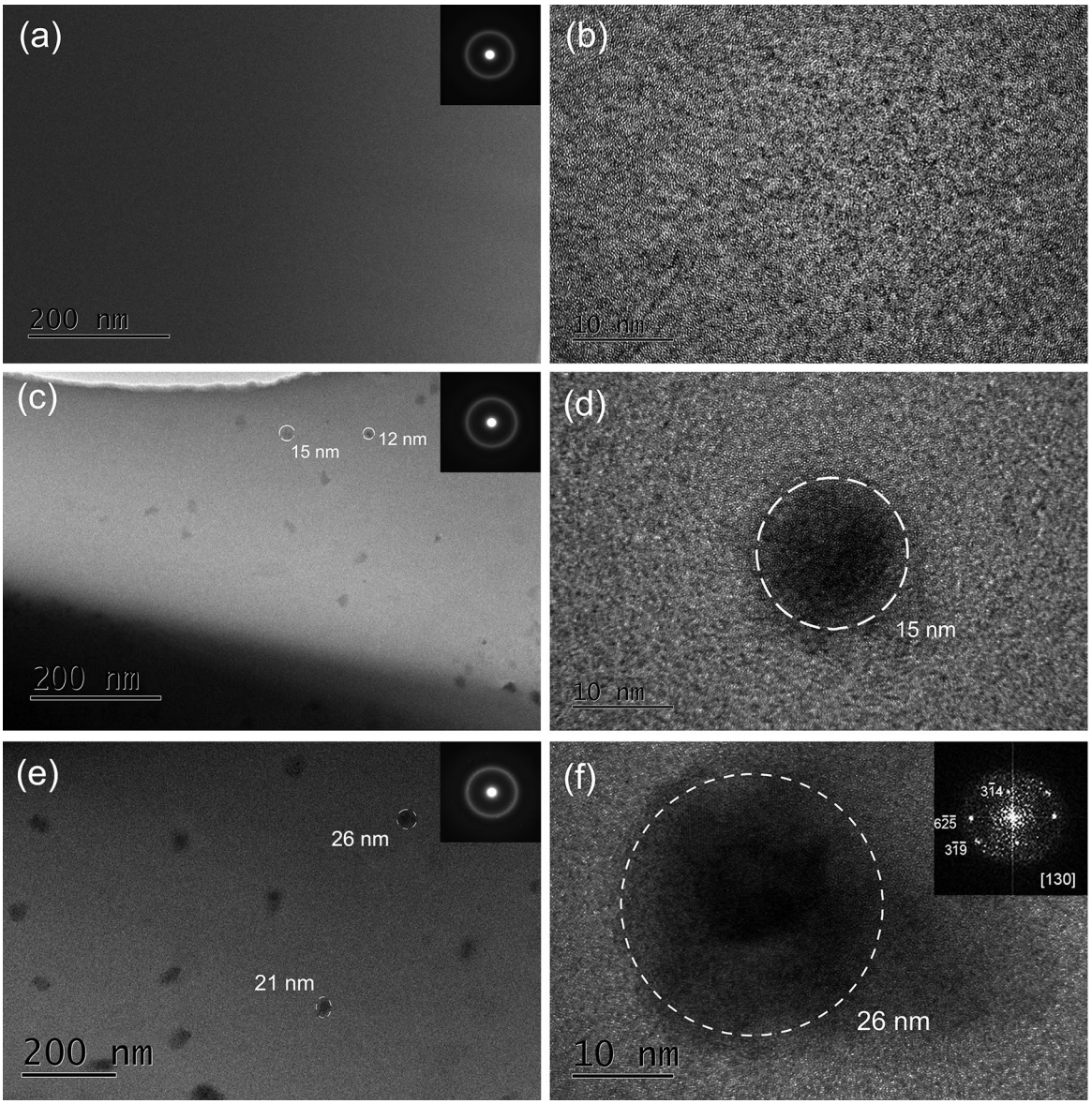

Figure 5. TEM images and corresponding SAED patterns and FFT of $(Cu_{47}Zr_{45}Al_8)_{97.5}Y_{1.5}Nb$ alloys treated at conditions: (a, b) untreated; (c, d) 680 K for 30 min; (e, f) 700 K for 30 min.

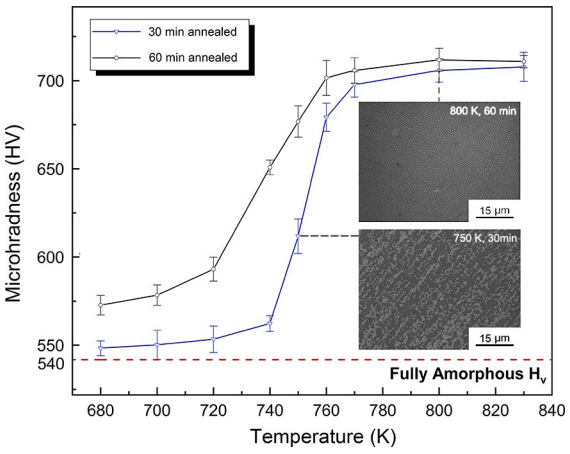

Figure 6. Microhardness curves of $(Cu_{47}Zr_{45}Al_8)_{97.5}Y_{1.5}Nb$ alloys and corresponding OM micrographs under different annealing processes.

larger dimension of the vein pattern (15~30 μm) than Figure 8 (b) does (5~10 μm). The smaller and denser veins in the sample after 700 K (427 ºC) annealing evidence that dispersed nanocrystals can inhibit the amorphous matrix from inhomogeneous rheological deformation[3]. In short, shear fracture mode remains in the amorphous alloys after annealing at 680~700 K (407 ºC~427 ºC) .

The heat treatment at 720 K (447 ºC) gives rise to multiple fracture characteristics rather than the single shear fracture mode, as collected in Figure 8 (c)~(e). Specially, Figure 8 (c) shows deep veins of nanoscale, while Fig. 8 (d) displays proliferating zone of shear bands. Furthermore, Figure 8 (c) presents both main shear bands parallel to the fracture surface and lateral shear bands along or perpendicular to those main

shear bands with a distance of 15 μm. The interlaced shear bands around fracture surface can well explain the tiny plastic strain shown in Figure 7.

The compressive property deteriorates dramatically upon raising the annealing temperature above 740 K. By then, the vein patterns that reflect the toughness of amorphous alloys have completely disappeared and been replaced by the river-like cleavage fracture patterns (Figure 9 (a)) and intergranular fracture patterns (Figure 9 (b)). Meanwhile, the fracture mode is transformed into brittle fracture. Alloy annealed at 760 K (487 ºC) shows the most inferior compression performance. Macroscopically, the fracture appears as sheet splitting, with fracture surfaces perpendicular to the loading direction, and the smooth swirling patterns further verify the characteristics of brittle fracture as shown in Figure 9 (c) and (d).

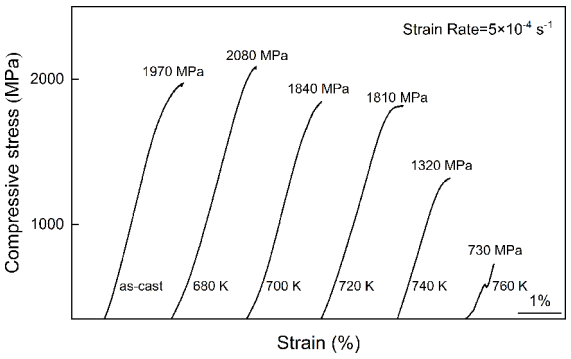

Figure 7. Uniaxial compression stress-strain curves of the samples annealed at different temperatures.

4. Discussion

XRD results of the $(Cu_{47}Zr_{45}Al_8)_{97.5}Y_{1.5}Nb$ BMGCs annealed for 60 min illustrate that the phase transformation upon temperature increase follows these steps:

Am (amorphous state) → Am + $Cu_{10}Zr_7$ → Am + $Cu_{10}Zr_7$ + $AlCu_2Zr$ + Al_2Zr

Formation of the precipitated phases is controlled by atomic diffusion and interfacial energy between these phases and the amorphous matrix. The more similar the structures of newly formed phase and matrix, the lower the interfacial energy between them, and the easier the nucleation of new phase[18]. According to the experimental results obtained, crystallization reactions begin with $Cu_{10}Zr_7$ formation and continue with the precipitation of $AlCu_2Zr$ and Al_2Zr; these three crystals coexist in the final state. It can be reasonably inferred that the $Cu_{10}Zr_7$ structure is much similar to the structure of amorphous matrix given that the Cu/Zr ratio in $Cu_{10}Zr_7$ resembles the nominal composition of the alloy most. Less atomic diffusion is required for the nucleation process, so that $Cu_{10}Zr_7$ precipitation dominates at lower annealing temperature [i.e. temperature lower than 740 K (467 ºC)]. Compared with the rate of Cu and Zr atoms (approximately 46/43) in Matrix, the nucleation of $AlCu_2Zr$

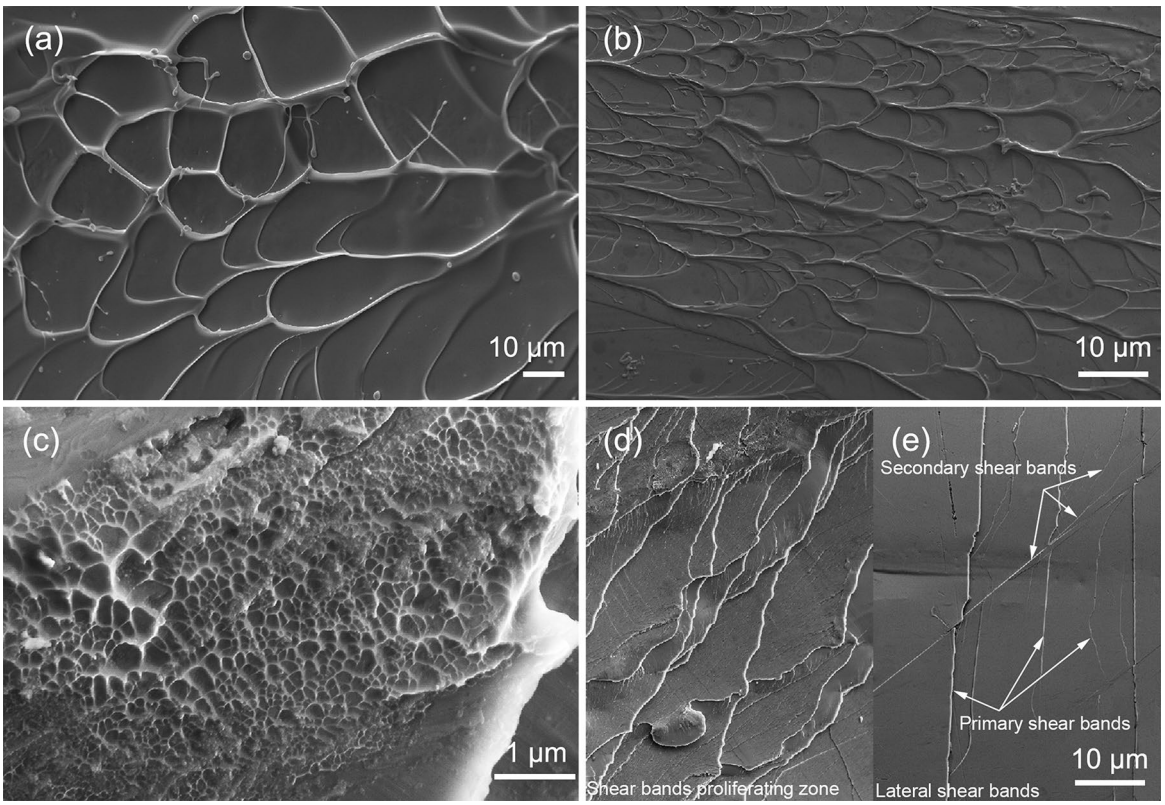

Figure 8. The fracture surface SEM images of the samples annealed at lower temperatures: (a), (b) vein patterns at 680 K, 700 K; (c), (d), (e) nanoscale vein patterns, frontal shear bands and lateral shear bands at 720 K.

or Al_2Zr depends on diffusion of Al atoms and releasing extra Zr/Cu atoms respectively, which puts forward higher demand for the atomic activity ability. As the temperature of 760 K (487 ºC) or above can well satisfy such activity capability, annealing under these conditions favours the nucleation of $AlCu_2Zr$ and Al_2Zr. Moreover, precipitation of these two phases accelerate the formation of Zr-rich/Al-poor and Cu-rich/Al-poor regions, which leads Cu and Zr atoms to accumulate in the vicinity, promotes the formation of $Cu_{10}Zr_7$, and ultimately conduces to the coexistence of three precipitates after 760 K (487 ºC) annealing.

In view of the crystallization behavior as well as the microhardness variation trend, isothermal annealing can exert a positive effect on the microhardness of $(Cu_{47}Zr_{45}Al_8)_{97.5}Y_{1.5}Nb$ BMGCs remarkably. In the temperature range of 680~720 K (407~447 ºC), structural relaxation that proceeds for long time causes the annihilation of free volume in amorphous matrix, thereby strengthening the atomic arrangement and enhancing the atomic binding force (Figure 10)[19,20]. In the meantime, the wide distribution of nano-sized phases in matrix can restrain the extension of shear bands, which improves the deformation resistance and thus the alloy microhardness. Annealing at higher temperatures (i.e. $T > 720$ K) leads to drastic crystallization that accounts primarily for the further enhancement in microhardness, and the maximum value of 712 HV remains unchanged after complete crystallization has been achieved (Figure 6).

Apparently, the alteration of alloy's mechanical properties is mainly ascribed to the second-phase particles that precipitate out in-situ during annealing. In the initial stage of amorphous crystallization, $Cu_{10}Zr_7$ with a 12~15 nm size benefits the compressive performance via dispersion strengthening[21],

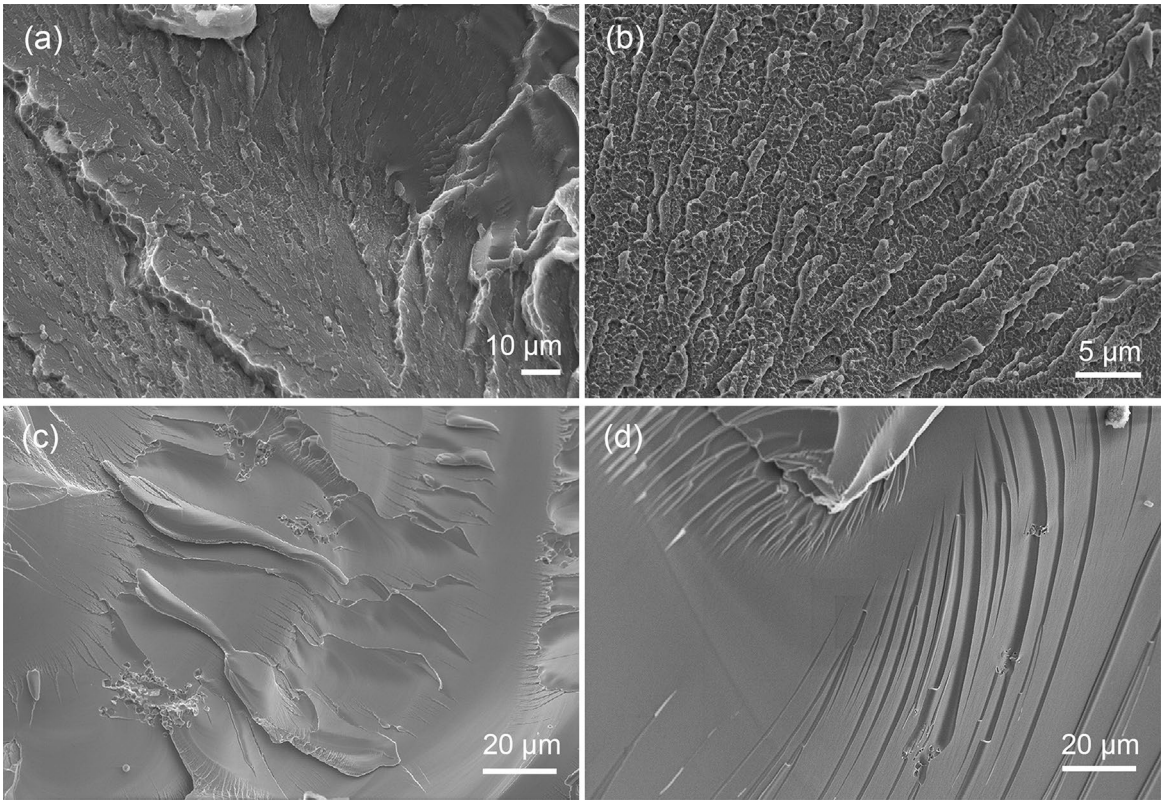

Figure 9. The fracture surface SEM images of the samples annealed at higher temperatures: (a), (b) 740 K; (c), (d) 760 K.

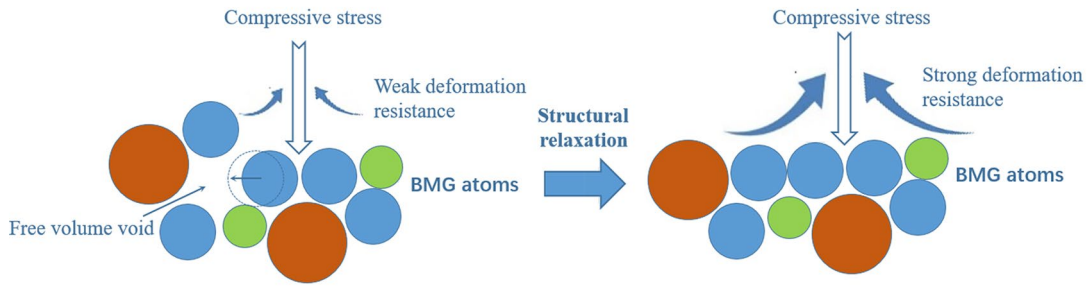

Figure 10. Diagram of structural relaxation strengthening mechanism.

such a congener strengthening mechanism also applies to Zr-based and Hf-based amorphous alloys[22,23]. Under this condition, the sizes and number density of dispersed crystals can not obviously prevent the rapidly propagation and highly-localization of the shear bands, and the alloy has no obvious plastic deformation but shear fracture directly. When raising the annealing temperature to 720 K (447 ºC), precipitates function as the nucleation agents in shear bands and trigger the generation of multiple shear bands (Figure 8 (d) and (e)), it can be considered that the sample has enhanced ductility and great potential for further plastic deformation under this condition. When the annealing temperature increase to 740 K (467 ºC), compression fracture mode of the alloy is then transformed from the typical amorphous fracture to crystalline brittle fracture, during which the metastable brittle Al_2Zr and $AlCu_2Zr$ phases precipitate out and dominate the fracture behaviour, accounting for the rapidly increasing brittleness. Stress concentrations on the crystalline/amorphous interface conduce to the initiation and propagation of microcracks, which ultimately causes brittle fractures in the alloys[24].

5. Conclusions

In this contribution, systematic investigations on the crystallization behavior in $(Cu_{47}Zr_{45}Al_8)_{97.5}Y_{1.5}Nb$ alloy help to establish and understand the relationship between annealing process, phase precipitation, and mechanical properties. The primary conclusions can be briefly summarized as follows:

1. Crystallinity of the $(Cu_{47}Zr_{45}Al_8)_{97.5}Y_{1.5}Nb$ BMGCs is positively correlated with the isothermal annealing time and temperature. The types and concentrations of crystalline phases increase with the annealing temperature, phase transformation upon temperature rise follows the procedure of Am (amorphous state) → Am + $Cu_{10}Zr_7$ →Am + $Cu_{10}Zr_7$ + $AlCu_2Zr$ + Al_2Zr.
2. Microhardness of the $(Cu_{47}Zr_{45}Al_8)_{97.5}Y_{1.5}Nb$ BMGCs is significantly improved with the deepening of crystallization. The sample annealed at 800 K for 60 min possesses Vickers hardness up to 712 HV, a 32% increase compared with that of the fully amorphous alloy. The nano-size $Cu_{10}Zr_7$ is beneficial to compressive properties, with the sample fracture strength increased to 2080 MPa after annealing at 680 K for 30 min. However, further increasing of temperature or extending of time causes sharp drop in the strength value.
3. Annealing at 680~700 K keeps the compressive fracture of $(Cu_{47}Zr_{45}Al_8)_{97.5}Y_{1.5}Nb$ BMGCs in the typical shear fracture mode. However, interlaced frontal and lateral shear bands are observed after 720 K annealing, while the cleavage and intergranular brittle fracture replaces shear fracture mode after 740 K annealing. Further raising the annealing temperature to 760 K leads to completely brittle fracture in the alloy.

6. Acknowledgements

This research is financially supported by the National Natural Science Foundation of China (Grant No.51301029 and 51375071).

7. References

1. Löffler JF. Bulk metallic glasses. *Intermetallics*. 2003;11(6):529-540.
2. Ketov SV, Sun YH, Nachum S, Lu Z, Checchi A, Beraldin AR, et al. Rejuvenation of metallic glasses by non-affine thermal strain. *Nature*. 2015;524(7564):200-203.
3. Sun BA, Wang WH. The fracture of bulk metallic glasses. *Progress in Materials Science*. 2015;74:211-307.
4. Inoue A, Takeuchi A. Recent development and application products of bulk glassy alloys. *Acta Materialia*. 2011;59(6):2243-2267.
5. Soto CEB, Vargas IAF, Velázquez JRF, Rodriguez GAL, Martínez JAV. Composition, Elastic Property and Packing Efficiency Predictions for Bulk Metallic Glasses in Binary, Ternary and Quaternary Systems. *Materials Research*. 2016;19(2):285-294.
6. Campos Neto ND, Paula WM, Pereira FS, Parrish CJ, Oliveira MF. Influence of Small Content Elements Additions on the Glass Forming Ability of Zr-based Bulk Metallic Glasses Alloys. *Materials Research*. 2018;21(6):e20171088.
7. Schroers J. Processing of bulk metallic glass. *Advanced Materials*. 2010;22(14):1566-1597.
8. Wang G, Guo CX, Pang SJ. Thermal stability, mechanical properties and corrosion behavior of a Mg-Cu-Ag-Gd metallic glass with Nd addition. Rare Metals. 2017;36(3):183-187.
9. Jiang QK, Wang XD, Nie XP, Zhang GQ, Ma H, Fecht HJ, et al. Zr-(Cu,Ag)-Al bulk metallic glasses. *Acta Materialia*. 2008;56(8):1785-1796.
10. Bai J, Wang J, Li L, Kou H, Li J. Thermal Stability and the Matrix Induced Brittleness in a Ti-based Bulk Metallic Glass Composite. *Materials Research*. 2015;18(Suppl 1):83-88.
11. Fan C, Yue XX, Inoue A, Liu CT, Shen XP, Liaw PK. Recent Topics on the Structure and Crystallization of Al-based Glassy Alloys. *Materials Research*. 2019;22(1):e20180619.
12. Zhang L, Chen S, Fu HM, Li H, Zhu ZW, Zhang HW, et al. Tailoring modulus and hardness of in-situ formed ß-Ti in bulk metallic glass composites by precipitation of isothermal ω -Ti. *Materials & Design*. 2017;133:82-90.
13. Yin J, Yuan GY, Chu ZH, Zhang J, Ding WJ. Formation, microstructure, and mechanical properties of in situ Mg-Ni-(Gd,Nd) bulk metallic glass composite. *Journal of Materials Research*. 2009;24(12):3603-3610.
14. Faith S, Bengisu Y, Ilkay K. Nanocrystallization in Cu-Zr-Al-Sm bulk metallic glasses. *Metallurgical and Materials Transactions A*. 2018;49(4):1328-1335.

15. Sun L, Wang J, Kou H, Li J, Zhang P. Phase Separation and Microstructure Evolution of $Zr_{48}Cu_{36}Ag_8Al_8$ Bulk Metallic Glass in the Supercooled Liquid Region. *Rare Metal Materials and Engineering*. 2016;45(3):567-570.

16. Liu D, Lin S, Ge S, Zhu Z, Fu H, Zhang H. A Ti-based bulk metallic glass composite with excellent tensile properties and significant work-hardening capacity. *Materials Letter*. 2018;233:107-110.

17. Liu CT, Heatherly L, Horton JA, Easton DS, Carmichael CA, Wright JL, et al. Test environments and mechanical properties of Zr-base bulk amorphous alloys. *Metallurgical and Materials Transactions A*. 1998;29(7):1811-1820.

18. Peng M, Dong C. Composition design and crystallization of Cu-Zr-Al-Ti metallic glasses. *Transactions of Materials and Heat Treatment*. 2011;32(6):37-44.

19. Huang Y, Zhou B, Chiu YL, Fan H, Wang D, Sun J, et al. The structural relaxation effect on the nanomechanical properties of a Ti-based bulk metallic glass. *Journal of Alloys and Compounds*. 2014;608:148-152.

20. Gu J, Zhang LX, Wang YH, Ni S, Guo SF, Song M. Combined effect of isothermal annealing and pre-compression on mechanical properties of Cu36Zr48Al8Ag8 bulk metallic glass. *Transactions of Nonferrous Metal Society of China*. 2016;26(6):1620-1628.

21. Apreutesei M, Esnouf C, Billard A, Steyer P. Impact of local nanocrystallization on mechanical properties in the Zr-59 at.% Cu metallic glass thin film. *Materials & Design*. 2016;108:8-12.

22. Qiu SB, Yao KF. Crystallization kinetics of Zr41Ti14Cu12.5Ni10Be22.5 bulk metallic glass in pulsing current pretreatment states. *Journal of Alloys and Compounds*. 2009;475(1-2):L5-L8.

23. Wang YT, Jiang FX, Wang YP, Zhan ZZ, Wang WK. Effect of heat treatment on mechanical properties of Hf-based amorphous alloy. *Transactions of Materials and Heat Treatment*. 2011;32(10):22-26.

24. Zhai HM, Wang HF, Liu F. Effect of minor Nb addition on mechanical properties of in-situ Cu-based bulk metallic glass composite. *Transactions of Nonferrous Metals Society of China*. 2017;27(2):363-368.